Fluid evolution and thermal structure in the rapidly exhuming gneiss complex of Namche Barwa–Gyala Peri, eastern Himalayan syntaxis

D. CRAW,[1] P. O. KOONS,[2] P. K. ZEITLER[3] AND W. S. F. KIDD[4]

[1]*Geology Department, University of Otago, PO Box 56, Dunedin, New Zealand (dave.craw@stonebow.otago.ac.nz)*
[2]*Department of Earth Science, University of Maine, Orono, ME, USA*
[3]*Earth and Environmental Science Department, Lehigh University, Bethlehem, PA 18015, USA*
[4]*Department of Earth & Atmospheric Sciences, University at Albany, Albany, NY, USA*

ABSTRACT   High-grade gneisses (amphibolite–granulite facies) of the Namche Barwa and Gyala Peri massifs, in the eastern Himalayan syntaxis, have been unroofed from metamorphic depths in the late Tertiary–Recent. Rapid exhumation (2–5 mm year^{-1}) has resulted in a pronounced shallow conductive thermal anomaly beneath the massifs and the intervening Tsangpo gorge. The position of the 300 °C isotherm has been estimated from fluid inclusions using CO_2–H_2O immiscibility phase equilibria to be between 2.5 and 6.2 km depth below surface. Hence, the near-surface average thermal gradient exceeds 50 °C km^{-1} beneath valleys, although the thermal gradient is relatively lower beneath the high mountains. The original metamorphic fluid in the gneisses was > 90% CO_2. This fluid was displaced by incursion of brines from overlying marine sedimentary rocks that have since been largely removed by erosion. Brines can exceed 60 wt% dissolved salts, and include Ca, Na, K and Fe chlorides. These brines were remobilized during the earliest stages of uplift at > 500 °C. During exhumation, incursion of abundant topography-driven surface waters resulted in widespread fracture-controlled hydrothermal activity and brine dilution down to the brittle–ductile transition. Boiling water was particularly common at shallow levels (< 2.5 km) beneath the Yarlung Tsangpo valley, and numerous hot springs occur at the surface in this valley. Dry steam is not a major feature of the hydrothermal system in the eastern syntaxis (in contrast to the western syntaxis at Nanga Parbat), but some dry steam fluids may have developed locally.

Key words: brine; fluid inclusions; Himalaya; hydrothermal; tectonics; thermal modelling; uplift.

INTRODUCTION

The Himalayan collision zone between India and Tibet has abundant shallow-level hot rocks that drive numerous meteoric hot spring systems (Fig. 1; Hochstein & Regenauer-Lieb, 1998). Most springs are on the Tibetan Plateau, where they define the Himalayan Geothermal Belt (Tong & Zhang, 1981; Hochstein & Regenauer-Lieb, 1998). The few springs in the high mountains are warm (< 50 °C), rather than hot (Fig. 1; Bhattarai, 1980; Craw, 1990; Hochstein & Regenauer-Lieb, 1998). The Main Central Thrust, near which these springs occur, has uplifted a zone of gneisses along much of the central Himalaya (Fig. 1; Gansser, 1964; Hubbard, 1989). Springs are locally emanating from these gneisses and footwall rocks beneath the thrust (Bhattarai, 1980; Craw, 1990; Hochstein & Regenauer-Lieb, 1998). The gneisses are being actively uplifted (Hodges *et al.*, 2004) and a shallow conductive thermal anomaly (cf. Koons, 1987) is probably providing the heat for the spring systems (Hochstein & Yang, 1995).

Hot springs also emanate from gneissic complexes in the high mountains of the Himalayan syntaxes at the eastern and western ends of the Himalayan mountain chain (Fig. 1), indicating elevated temperatures at shallow depths in these regions as well (Hochstein & Regenauer-Lieb, 1998; Zeitler *et al.*, 2001). The thermal structure and nature of fluid evolution during uplift of gneisses at Nanga Parbat in the western syntaxis (Fig. 1) has been examined previously by Winslow *et al.* (1994), Craw *et al.* (1994, 1997) and Chamberlain *et al.* (2002). These studies have shown that boiling fluids occur through large volumes of shallow rocks, including surface springs, and meteoric water penetrates readily to a shallow (*c.* 8–10 km below surface) brittle–ductile transition. Nanga Parbat is one of the few natural geothermal areas on Earth to have high rock temperatures at sufficiently shallow levels to generate dry steam (Craw *et al.*, 1997). This spectacular thermal anomaly is generated by rapid uplift from metamorphic depths of gneissic rocks, driven by localized orogen-parallel shortening in the syntaxial zone and
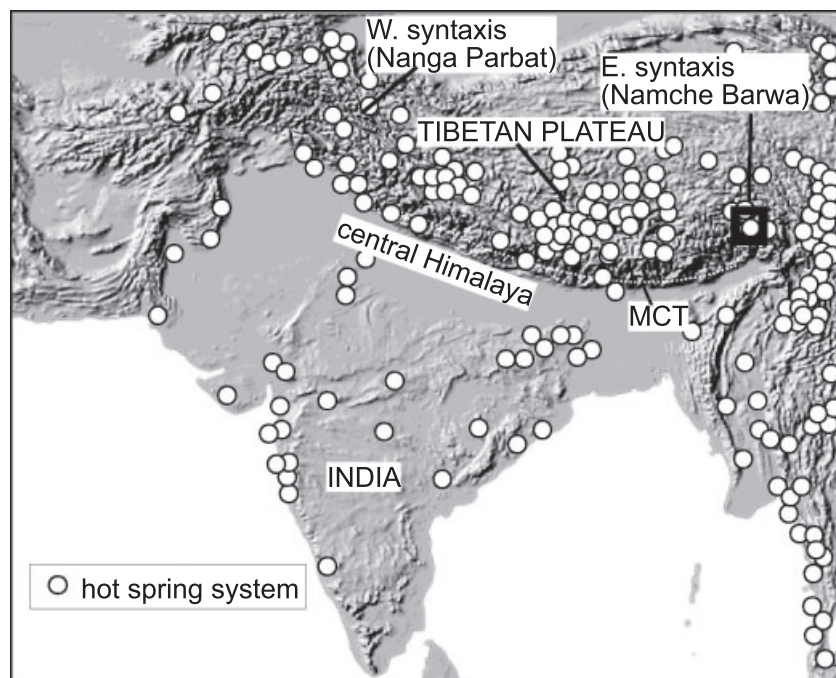

Fig. 1. Digital elevation model of the Himalayan region (from US Geological Survey), showing the locations of the eastern and western syntaxes, and the Main Central Thrust (MCT) in the central Himalaya. The main Himalayan mountain chain follows, and lies immediately north of, the MCT. Principal hot spring systems are indicated (after Hochstein & Regenauer-Lieb, 1998).

deep river erosion (Zeitler *et al.*, 2001; Koons *et al.*, 2002).

Hot springs are the surface expressions of more complex fluid systems at depth during active mountain-building in the Himalaya, and evidence of the nature of a fluid system at depth is progressively exposed during exhumation (Pecher, 1979; Boullier *et al.*, 1991; Chamberlain *et al.*, 2002). The fluid compositions, and thermal structure of the fluid systems, also evolve with time as progressively higher-grade metamorphic rocks are exhumed, commonly with an evolving shallow crustal thermal anomaly (Craw *et al.*, 1997; Chamberlain *et al.*, 2002). Fluid flow and compositional evolution is a significant part of the tectonic process (Boullier *et al.*, 1991), and one that is difficult to interpret in studies of metamorphic rocks in the roots of ancient mountain belts. Hence, studies of fluids and fluid evolution in active mountain belts provide important information on processes in modern and ancient orogenic belts.

The present study provides the first data on the fluid and thermal structure of the uplifting gneiss complex of Namche Barwa, in the eastern Himalayan syntaxis (Fig. 1). Unlike the western syntaxis, the Namche Barwa area is difficult to access and little previous work has been published on thermal aspects of this region. We present observations on the structural nature of veins formed by fluids in the gneiss complex during exhumation and uplift, and describe the fluids observed in fluid inclusions in these veins. From these data, we estimate temperatures and depths of fluid entrapment and consequently can estimate local thermal gradients in the gneiss complex. We also document the compositional evolution of fluids within the gneiss complex during uplift, and compare these fluids to those seen elsewhere in the Himalaya.

GEOLOGY OF THE EASTERN HIMALAYA

The high mountains of the central Himalaya are made up mainly of Mesozoic Tethyan carbonate-clastic sedimentary rocks, and gneisses overlying the Main Central Thrust (Fig. 1), that have been intruded by granitoids (Gansser, 1964). This structural sequence continues eastwards, but the Tethyan sedimentary rocks become strongly attenuated immediately before the eastern syntaxis, which is a well-defined re-entrant in the mountain chain at the eastern end of the Himalaya (Fig. 1). The most prominent topographic features of the syntaxis are the peaks of Namche Barwa (7782 m) and Gyala Peri (7294 m) that stand higher than other Himalayan mountains immediately to the south-west. These high mountains are separated by the deeply incised gorge of the Yarlung Tsangpo as that north-east trending river is joined by the Po Tsangpo and bends sharply southwards (Fig. 2). This spectacular topography, including some of the deepest gorges on Earth, is cut into a gneiss complex that has been exhumed from metamorphic depths over the past 10 Myr (Burg *et al.*, 1997, 1998; Booth *et al.*, 2004).

The gneiss complex consists of upper amphibolite to granulite facies metasedimentary gneisses, and granitoid and mafic orthogneisses, some of which were initially metamorphosed in the middle Tertiary or earlier (Booth *et al.*, 2004). These core gneisses (Fig. 2) have higher metamorphic grade than surrounding
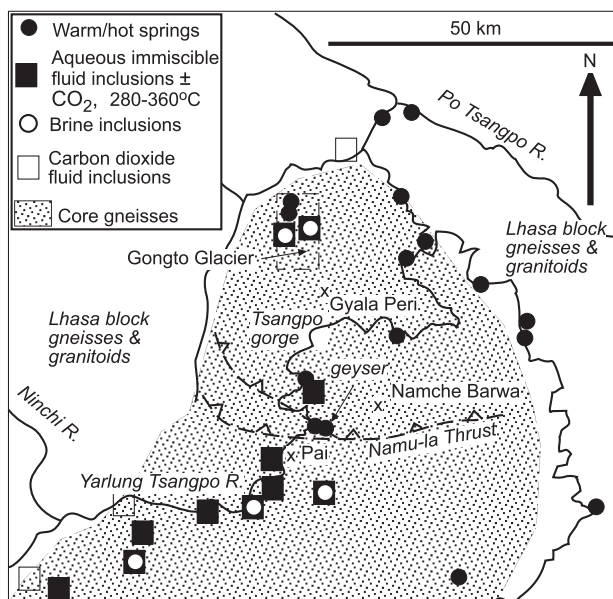
Fig. 2. Map of the Namche Barwa and Gyala Peri massifs in the eastern Himalayan syntaxis, with distribution of principal fluid features. Hot spring locations are partly from Zhang *et al.* (1992). Compositions of fluid inclusions in quartz veins are summarized from Table 1.

Fig. 3. Geological sketch map of the Gongto Glacier area, on the north side of Gyala Peri (Fig. 2). Outcrop sample localities for fluid inclusion studies are indicated, and additional samples were collected from glacier moraines.

rocks of the Lhasa block that include largely meta-sedimentary greenschist to amphibolite facies gneisses metamorphosed in the early–middle Tertiary, and largely undeformed batholithic granitoids (Burg *et al.*, 1997, 1998; Liu & Zhong, 1997). Metasediments in the gneissic core are dominated by migmatites and meta-pelites (commonly sillimanite-bearing), with minor quartzite, marble, and diopsidic calc-silicate rocks. The gneissic core is separated from the surrounding lower-grade rocks by a complex set of faults and ductile shear zones (Burg *et al.*, 1997, 1998; Liu & Zhong, 1997). The core itself is disrupted by faults and ductile shear zones that juxtapose 10 km scale domains of differing lithology and metamorphic grade (Burg *et al.*, 1997, 1998; Liu & Zhong, 1997). Smaller (km scale) structurally and lithologically distinct domains can be mapped locally as well (Fig. 3). The Namu-la Thrust (Liu & Zhong, 1997) is one of the most prominent structures cutting the core gneisses (Fig. 2). Thrust faults in gneisses near to this fault zone (west of Pai, Fig. 2) show progressive change from mainly ductile strain under amphibolite facies conditions, through brittle and ductile strain with greenschist facies assemblages, to near-surface variably cemented fault gouges.

Numerous warm and hot springs emanate from bedrock and/or overlying Quaternary sediments in and near the core gneisses (Figs 2 & 3; Zhang *et al.*, 1992). These springs occur mainly in the Tsangpo gorge (Fig. 1), although two appear to be fault-controlled in a hanging valley on the north-west slopes of Gyala Peri
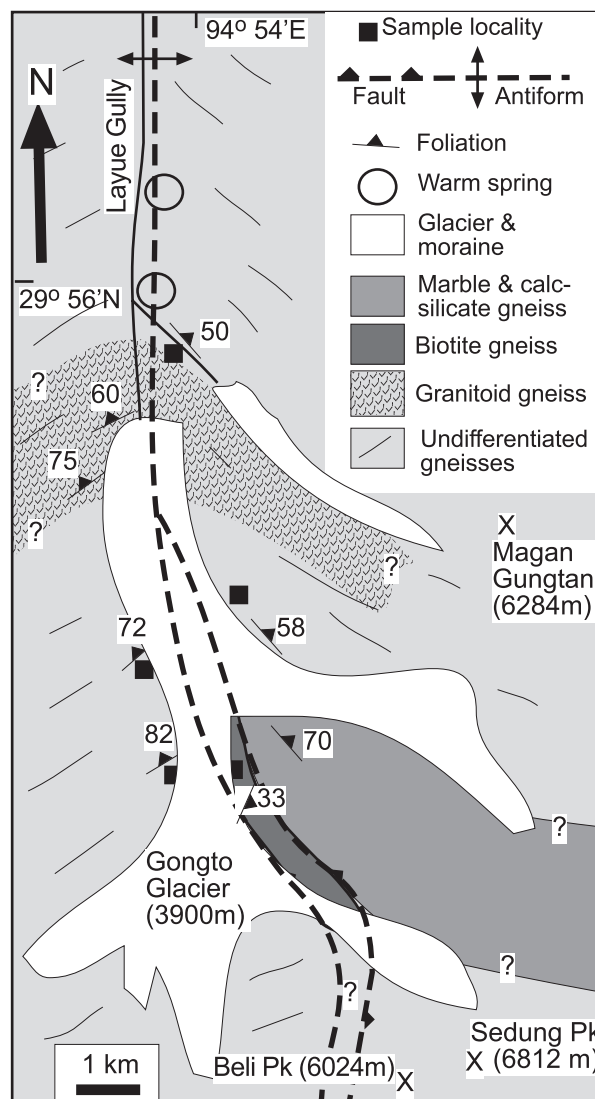
(Fig. 3). Spring temperatures range from 35 to 85 °C, with one geyser reported (Fig. 2; Zhang *et al.*, 1992). Calcite is being actively deposited from many of these springs at the surface.

QUARTZ VEINS IN GNEISSES

Quartz veins occur sporadically in the core gneisses, in a range of structural settings: synmetamorphic, late-metamorphic and post-metamorphic, with respect to the pervasive foliation and related metamorphic minerals. Synmetamorphic veins are the most common. These 1–10 cm thick veins have been deformed and boudinaged with the enclosing foliated gneiss, although many of these veins cut the gneissic foliation
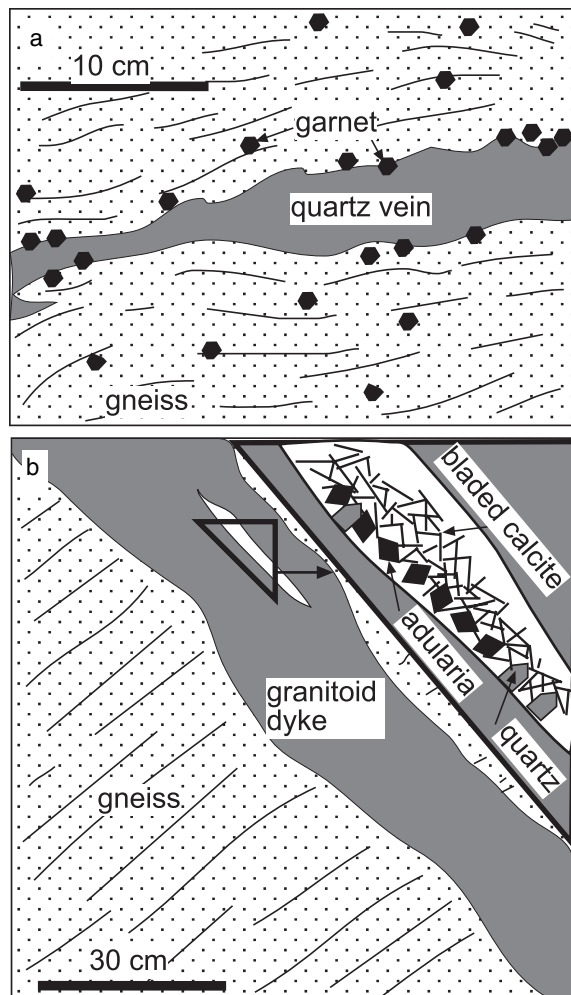
Fig. 4. Sketches (from photographs) of outcrops of quartz veins sampled for fluid inclusion studies. (a) Quartzofeldspathic gneiss with boudinaged foliation-parallel quartz vein, Gongto Glacier (Fig. 3). Coarse-grained garnet has grown in gneiss and quartz vein. (b) Large cavity (white, with triangle showing inset sketch area) has developed in a late-stage granitoid dyke within high-grade gneiss, north bank Yarlung Tsangpo, Pai. The cavity is partially filled with bladed calcite and euhedral quartz and adularia, as sketched in the triangular inset in top right.

Fig. 5. Sketches (from photographs) of outcrops of high-grade gneisses in a thrust fault, Yarlung Tsangpo valley, 5 km west of Pai, showing localized post-metamorphic hydrothermal alteration and fault disruption. Fluid inclusion studies were conducted on quartz from veins (black).

at a low angle. These veins are most abundant in biotite-rich metasedimentary gneisses in the Gongto Glacier area (Figs 3 & 4a), and are relatively rare in the gneisses on the slopes of Namche Barwa. Deformed lenses (cm scale) of quartz locally occur in boudin necks where feldspathic rocks have been boudinaged between micaceous gneiss horizons. All these deformed veins contain metamorphic minerals such as garnet (Fig. 4a), hornblende or biotite, along their margins. The quartz in these veins has recrystallized during metamorphism, and has a uniform granoblastic texture in most veins.

Late-metamorphic quartz veins clearly cut the gneissic foliation, but have also been weakly deformed
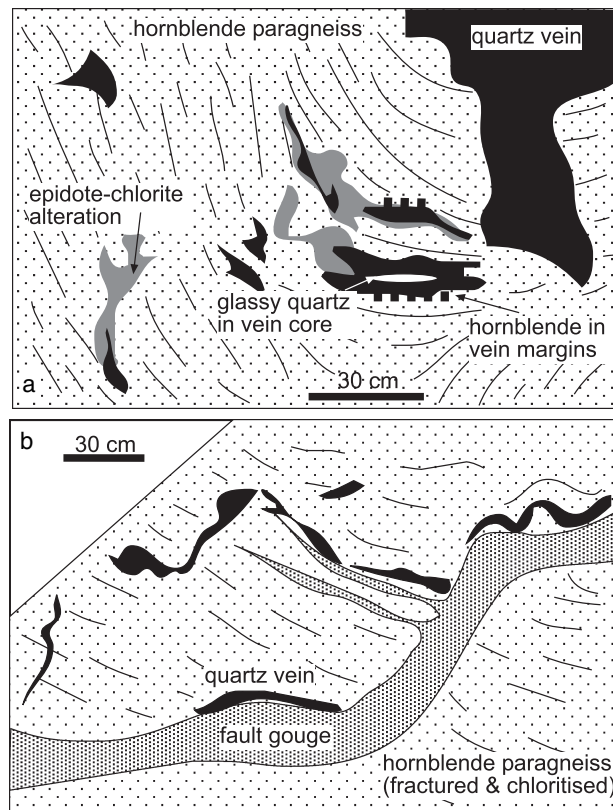
with that foliation (Fig. 5a). These veins are up to 50 cm across in places, but are discontinuous laterally and generally form irregular patches within the gneiss (Fig. 5a). These veins are most common in thrust faults west of Pai (Fig. 2), and become rare upstream and within the gorge farther downstream. The veins are made up of milky quartz, and commonly have coarse-grained (cm scale) hornblende on their margins (Fig. 5a), locally with biotite and cm-scale euhedral titanite grains. The veins have been overprinted by later hydrothermal activity that has resulted in patchy alteration of hornblende and biotite to epidote and chlorite in vein margins and adjacent host rock (Fig. 5a). In addition, some fractures in the original milky quartz veins have been filled with late-stage glassy anhedral quartz (Fig. 5a) with enclosed epidote and chlorite. Both milky and glassy quartz have been subsequently deformed into open to tight folds and irregular angular pods adjacent to low-angle faults with well-defined gouge zones. These gouge zones are cemented with calcite and authigenic clays altered from chlorite, muscovite and biotite (Fig. 5b).

One set of localities at the upstream entrance to the Yarlung Tsangpo gorge (west of Pai and outside the

thrust fault zones) has moderately to steeply dipping open fractures (2–8 cm wide) partially filled with post-metamorphic hydrothermal quartz, calcite and adularia (Fig. 4b). The quartz is prismatic (up to 2 cm long) and adularia crystals are euhedral (0.5–1 cm across). The calcite is platy and/or bladed, and forms an interlocking network of crystals around the quartz and adularia (Fig. 4b, inset). These mineralized fractures have sharp margins and cut across all rock types (including dykes, Fig. 4b) and the gneissic foliation.

Veins are rare in the lower-grade gneisses around the margin of the gneissic core, and consist of fine-grained (< < 1 mm) milky quartz in irregular fractures parallel to, and locally crosscutting, the pervasive foliation. Quartz in these veins is fully recrystallized and has a granoblastic texture.

METHODS

Samples for this study were collected from quartz veins in natural exposures and in road cuts, at sites indicated in Fig. 2. Natural exposures in vegetated areas are commonly covered in moss and lichen and consequently are partially weathered, and thin section observations are masked by alteration products. Hence, boulders immediately below natural outcrops were sampled as well. Lateral moraines of the Gongto Glacier (Figs 2 & 3) provided some clean specimens of material essentially identical to that exposed in vegetated outcrops nearby. Reconnaissance petrographic and microthermometric studies have shown that there are no major differences between samples from boulders and samples from outcrops. However, it was not possible to make detailed microthermometric observations on some outcrop samples, and boulder material was used instead.

Slices of clean quartz specimens were ground to $c.$ 100 μm thick and polished on both sides. The resultant polished wafers were examined with a standard petrographic microscope, and microthermometrically using equipment and techniques described by Craw *et al.* (1994, 1997). A summary of microthermometric data is presented in Table 1. Ranges of temperature data are derived from 10 to 30 individual measurements on the same generations of inclusions in $c.$ 2 mm^2 of polished quartz. Visual estimates of volumetric proportion of CO_2 component of mixed CO_2–H_2O inclusions were obtained from area proportions in digital images, facilitated by comparative diagrams (Roedder, 1984). Estimates of fluid composition were obtained using phase diagrams documented by Schwartz (1989), Blencoe *et al.* (2001), Bakker & Diamond (2000) and Diamond (2001, 2003) (mixed water–carbon dioxide), Vanko *et al.* (1988), Bodnar *et al.* (1989) and Bodnar (2003) (brines), and computer packages MacFlincor (Brown & Hagemann, 1995) and FLUIDS (Bulk) (Bakker & Brown, 2003). Saline fluid inclusions with daughter crystals in material from the

Gongto Glacier area (Fig. 3) were analysed *in situ* using a JEOL 8600 electron microprobe by a technique described by Maaskant (1986). Analyses were conducted by wavelength dispersion at 30 kV with 2 μm beam size on carbon-coated polished quartz, and data were reduced using standard ZAF correction.

FLUID INCLUSIONS

A wide range of fluid inclusion compositions is apparent from petrography of the samples obtained from the eastern syntaxis. Primary inclusions are rare, but are found sporadically in all generations of quartz veins. These inclusions are equant and are isolated in clear patches of quartz. Primary inclusions in metamorphic veins from the Gongto Glacier area and Namche Barwa (Figs 2 & 3) occur entirely enclosed within recrystallized quartz grains. Hence, these inclusions are not primary with respect to initial vein formation; they are primary with respect to the latest stage of quartz recrystallization only. Any fluid inclusions from the time of the formation of these veins have been destroyed by this recrystallization. Subsequent deformation has affected vein margins only, and the inclusions used for this study were sampled from the undeformed interior of these veins. Likewise, younger generations of veins from the Tsangpo valley commonly have some minor shearing around their margins, but samples for this study were taken from undeformed interiors of veins. Primary inclusions in these veins are undeformed and have no evidence for post-entrapment modification (cf. Roedder, 1984).

Most of the observed inclusions are secondary, are elliptical or irregular in shape, and occur in healed fractures cutting across quartz grains. Inclusion trails in some samples have been truncated by post-entrapment fractures, but there is no evidence for deformation of inclusions near to these fractures. Inclusion compositions are highly variable between adjacent secondary inclusion trails (10–20 μm scale). Inclusion necking can cause variations in composition of the type observed (Roedder, 1984). However, no necking textures (cf. Roedder, 1984) have been identified. The widespread and consistent occurrence of these coexisting inclusion types (Table 1; Fig. 2) suggests that localized necking can be discounted in this study.

For the purposes of the present study, we are concerned with broad compositional groupings and general fluid evolutionary trends. Hence, sets of inclusions in each general vein type are grouped on the basis of relative timing and composition. A primary generation and two to four sets of secondary generations can be identified in each vein type, as listed in Table 1, and pictured in Figs 6 and 7. There are many similarities between some generations in different vein types and locations, and these are mentioned in the following descriptions, using the generation label listed in the first column of Table 1. For each vein type in Table 1,

Table 1. Summary of microthermometric data (°C) for fluid inclusions in the eastern Himalayan syntaxis core gneiss complex.

Generation	Composition	Mode	Host quartz	Eutectic	Ice	Clathrate	CO_2 homog.	Daughter	Salt homog.	Final homog.	Density (g cm^{-3})
Lhasa Block syn- to late-metamorphic quartz veins, outside core gneiss complex											
LBL 2	CO_2	2°					0–5			nv	0.9
Gongto Glacier synmetamorphic quartz veins in core gneisses											
GGS 1	Concentrated brine	1°	White quartz (d)	nv	nv			Multiple	460–490	500–515	0.75
GGS 2a	Brine	2°	White quartz (d)	−23				NaCl, KCl	150–250	310–350	0.65–0.75
GGS 2b	Mixed CO_2–H_2O	2°	White quartz (d)		0	10	27–31(v)			280–320	0.2–0.5
	Water (coexist)			−23	nv			NaCl, KCl	190–240	285–310	0.65–0.75
GGS 2c	Saline water	2°	White quartz (d)	−23 to < −37	−3 to −15	nv				245–365	0.6–0.75
Namche Barwa gneiss synmetamorphic quartz veins in core gneisses											
NBS 1	Brine	1°	Glassy quartz (d)	−23	0			NaCl, KCl	200–250	290–355	0.6–0.75
NBS 2a	Mixed CO_2–H_2O	2°	Glassy quartz (d)		−3 to −5	10	27–30(v)			280–320	0.2–0.5
	Water (coexist)			−22	−3 to −5	6–8				290–315	0.7
NBS 2b	Water	2°	Glassy quartz (d)	−23	−3 to −5	nv	12–15(v)			280–320	0.1–0.2
Thrust fault hosted late-metamorphic veins, Yarlung Tsangpo valley											
FZLM 2	Mixed CO_2–H_2O	2°	Milky quartz(d)		0	10	27–30(v)			290–330	0.2–0.5
	Water (coexist)				−3 to −5	6–8				270–320	0.7
FZLG 1	Mixed CO_2–H_2O	1°	Glassy quartz(w)		0	10	27–30(v)			290–310	0.2–0.5
	Water (coexist)				−3 to −5	6–8				280–325	0.7
FZLG 2a	Mixed CO_2–H_2O	2°	Glassy quartz(w)		0	10	27–30(v)			280–320	0.2–0.5
	Water (coexist)				−3 to −5	6–8				290–310	0.7
FZLG 2b	Mixed CO_2–H_2O	2°	Glassy quartz(w)		−3	10	28–31(l)			280–300	0.5–0.6
	Water (coexist)				0	−7				290–300	0.7
FZLG 2c	Water vapour	2°	Glassy quartz(w)	0	0 to −3	nv				245–365	0.02–0.16
	Water (liquid, coexist)					nv				250–320	0.7–0.8
FZLG 2d	Water vapour, minor CO_2	2°	Glassy quartz(w)		nv	10	11–16(v)			280–320	0.1
PHP 1	Water liquid	1°	Quartz crystals(u)	−23	−3 to −4					290–295	0.7
PHP 2a	Water vapour	2°	Quartz crystals(u)		0	nv				288–310	0.05
	Water (liquid, coexist)				0					290–296	0.7
PHP 2b	Water, minor CO_2	2°	Quartz crystals(u)		0	10	12–15(v)			280–320	0.1

Homog., homogenization temperature; nv, not visible; (v), homogenization to vapour; (l), homogenization to liquid; 1°, primary; 2°, secondary; (d), deformed during metamorphism; (w), weakly deformed; (u), undeformed.
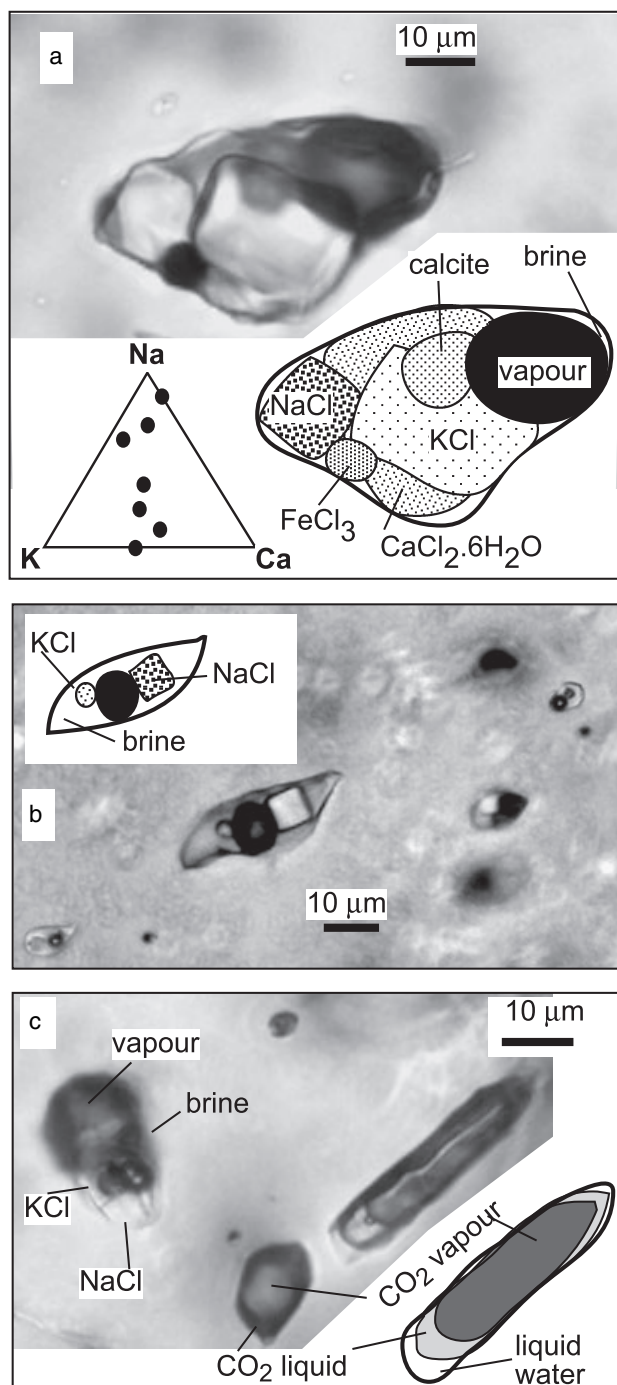
Fig. 6. Photomicrographs of fluid inclusions in a foliation-parallel quartz vein from the Gongto Glacier area (Fig. 3). (a) Primary brine inclusion, with daughter minerals identified by microprobe, as indicated in the accompanying sketch. Inset shows proportions of principal chemical components of the brine, from microprobe analyses. (b) Secondary brine inclusion, with daughter minerals indicated in the accompanying sketch. (c) Coexisting brine and CO_2-rich secondary inclusions.

the generations are presented in order of decreasing relative age, except where this is not known (as noted in the descriptions).

Gongto Glacier synmetamorphic veins

Primary fluid inclusions are characterized by abundant daughter crystals, with some inclusions containing so much crystalline material that the liquid component is almost completely obscured (Fig. 6a). These saline inclusions were the only ones to allow estimation of composition by microprobe, and only small (*c.* 10 μm) inclusions in one sample yielded results. The microprobe detected Na, Ca, K, Fe, Cl, and a trace of sulphur. These results, combined with standard microscope petrography, allow tentative identification of the principal daughter crystals (Fig. 6a; cf. Roedder, 1984; Bodnar, 2003). The detected sulphur may be in gypsum, but this has not been confirmed. The distinction between halite and sylvite can also be readily determined during heating, when halite displays retrograde solubility (Bodnar, 2003). Semiquantitative analytical results from inclusions (Fig. 6a) show a wide range of proportions of Na, Ca, and K, with the Na content varying most widely. Some of this variation may be a result of preferential absorption of X-rays from Na by the quartz host (Maaskant, 1986; Anderson & Mayanovic, 2003). However, petrographic observations of these primary inclusions show that halite crystal proportions are highly variable within samples on the mm scale, and halite clearly dominates in some inclusions as the analytical data imply (Fig. 6a, inset).

Primary concentrated brine inclusions from the Gongto Glacier area homogenize by disappearance of the vapour bubble at 500–515 °C, and the last daughter crystal (halite or sylvite) dissolves at 460–490 °C (GGS 1; Table 1). Phase diagrams for the complex system represented by assemblages such as those of Fig. 6(a) are not available, but by analogy with simpler systems (Vanko *et al.*, 1988; Bodnar *et al.*, 1989), the salinity of these inclusions is up to 60 wt%. Bulk density, estimated by the method and software described by Bakker & Brown (2003), is *c.* 0.75 g cm^{-3}. We conclude that the fluid which accompanied synmetamorphic quartz recrystallization was highly saline brine with variable compositions.

The Gongto Glacier synmetamorphic veins are cut by numerous generations of secondary inclusion trails. Inclusions are commonly elongate along the trails, and occur in planes that cut across the recrystallized quartz fabric. The earliest generations of these secondary trails contain small vapour bubbles and two daughter crystals, and have apparently uniform composition along individual trails (Fig. 6b). Temperatures of first observed melting were between −20 and −25 °C, although this was difficult to resolve in the small inclusions. It was not possible to determine the components of the salinity in these inclusions with the microprobe. However, first melting temperatures, petrography and retrograde solubility observations (see above) suggest that the daughter crystals are halite and sylvite. The secondary brine inclusions homogenize by vapour disappearance at 310–350 °C (GGS 2a; Table 1). Sylvite dissolves at *c.*
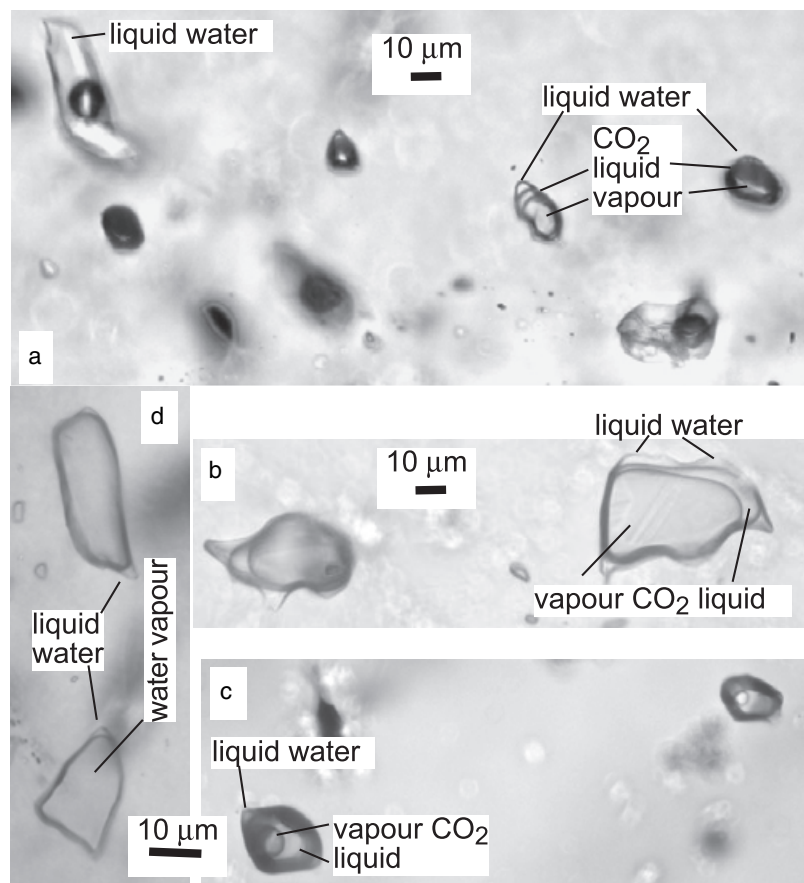
Fig. 7. Photomicrographs of fluid inclusions from glassy quartz in an outcrop of late-metamorphic quartz vein in a thrust fault zone, Yarlung Tsangpo valley, 5 km west of Pai (Fig. 2). (a) Vapour-rich water inclusions. (b) Coexisting liquid water and CO_2 vapour-rich primary inclusions. (c) CO_2-rich vapour-dominated inclusions. (d) CO_2-rich liquid-dominated inclusions.

150–190 °C and halite finally dissolves at 200–250 °C (Table 1). These results imply salinities of 30–35 wt% (Bodnar, 2003).

The secondary brine inclusion trails are crosscut by trails of inhomogeneous secondary inclusions. These trails contain some brine inclusions of the type described above, but the trails are dominated by elongate inclusions with carbon dioxide liquid and vapour with only minor liquid water phase (Fig. 6c). The proportions of CO_2 liquid and vapour are variable within these trails (Fig. 6c). Most of the mixed H_2O–CO_2 inclusions are dominated by CO_2 vapour, and the liquid CO_2 annulus homogenizes to vapour between 27 and 30 °C (GGS 2b; Table 1). The most vapour-rich CO_2–H_2O inclusions finally homogenize between 280 and 320 °C (GGS 2b; Table 1). Coexisting brine inclusions in the same trails homogenize between 285 and 310 °C. These homogenization data and visual estimates of volumetric proportion of CO_2 component imply bulk inclusion composition of 40–50 mol.% CO_2, and fluid density between 0.2 and 0.5 g cm^{-3} (Fig. 8a; Schwartz, 1989). Some mixed water–CO_2 inclusions from these trails homogenize at higher temperatures (up to 400 °C), and some of these inclusions decrepitate before homogenization. The wide range of inclusion compositions observed in these secondary trails is characteristic of fluid immiscibility during entrapment (Roedder, 1984; Craw *et al.*, 1993).

The latest secondary generation in the Gongto Glacier quartz veins consists of trails of irregularly shaped large (> 50 μm) water inclusions. Most of these inclusions are dominated by water vapour, but some are dominantly liquid water. These two types coexist in many trails. The water inclusions homogenize between 245 and 365 °C, with coexisting liquid- and vapour-rich inclusions homogenizing at similar temperatures in this range (GGS 2c; Table 1). Some vapour-rich inclusions in these trails had not homogenized at 400 °C when the larger and more irregular-shaped ones began to decrepitate. The liquid-dominated inclusions do not contain daughter minerals, but have ice-melting temperatures as low as −15 °C, implying salinity of up to 19 wt% NaCl (equivalent) (Bodnar, 2003). Eutectic melting was not clearly observed in any of these inclusions, but this occurred below −37 °C. Inclusions with similar appearance in some of the same samples have ice-melting temperatures between −3 and −5 °C, and eutectic melting near −23 °C. The eutectic melting data imply that the more saline of these inclusions contain at least some $CaCl_2$, and the more dilute solutions contain NaCl and KCl only (Roedder, 1984; Bodnar, 2003).
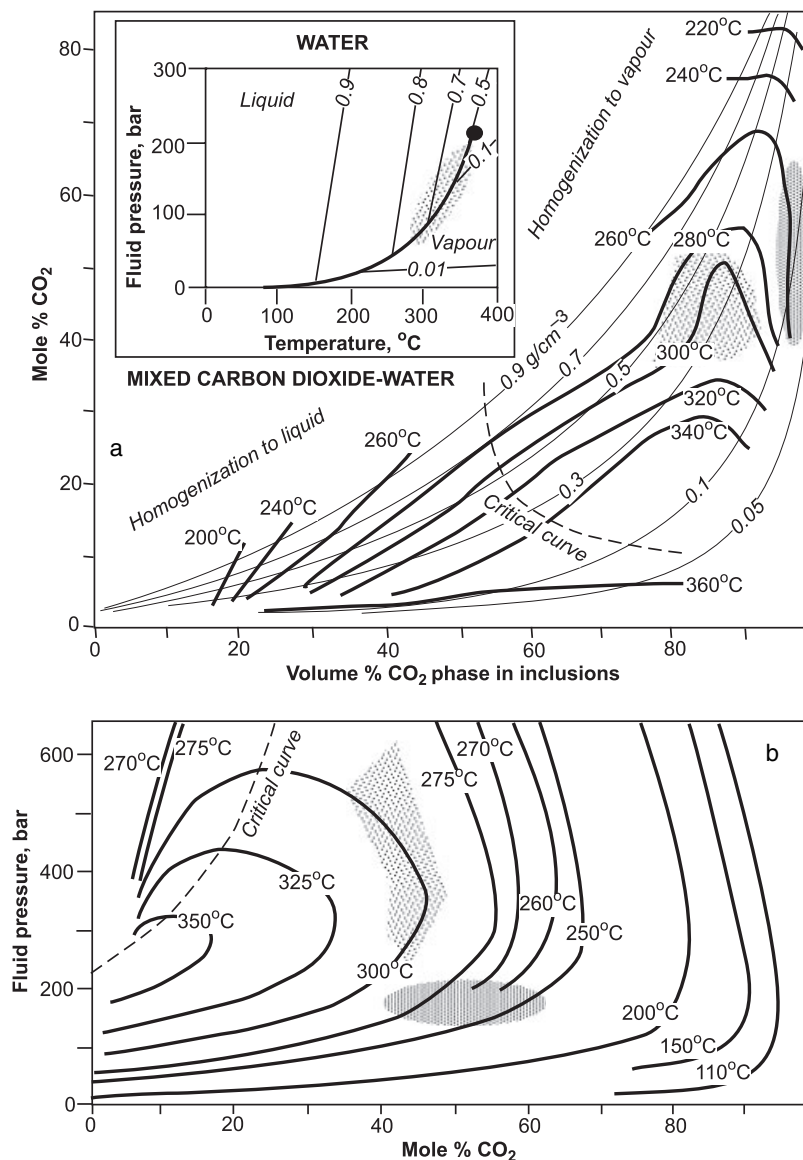
Fig. 8. Phase diagrams for fluid equilibria discussed in the text. See text for sources. Stippled areas represent ranges of compositions commonly observed in the Namche Barwa and Gyala Peri massifs, and are the basis for estimates of fluid pressures and temperatures. (a) Diagram for mixed carbon dioxide and water vol.% CO_2 v. mol.% CO_2 for fluid inclusions. Inset shows pure water temperature v. fluid pressure. (b) Mol.% CO_2 v. fluid pressure for mixed carbon dioxide and water fluids.

Namche Barwa synmetamorphic veins

Primary inclusions in these veins are, like those of the Gongto Glacier area (above), primary with respect to quartz recrystallization, not vein formation. The easiest observed primary inclusions are in glassy quartz in boudin necks (see above), as most synmetamorphic veins are fine grained and milky in appearance, precluding detailed inclusion study. Primary inclusions are rare, even in the glassy quartz, and consist of brines with small vapour bubbles and two daughter crystals that are inferred (see Methods) to be halite (dominant) and sylvite (subordinate). Sylvite dissolution temperatures were difficult to resolve because of small crystal size, but the halite dissolves at 200–250 °C and the inclusions homogenize by vapour disappearance between 290 and 355 °C (NBS 1; Table 1), similar to comparable inclusions in Gongto Glacier samples

(GGS 2a; Table 1). These observations imply salinities of c. 30–35 wt% (Bodnar, 2003).

Most inclusions in Namche Barwa gneisses occur in secondary inclusion trails, which cut the recrystallized quartz veins, including glassy quartz in boudin necks, at a wide variety of angles. These trails consist mainly of elongate inclusions containing mixtures of water and carbon dioxide, similar to those described above (Fig. 6c). The mixed CO_2–H_2O inclusions are almost invariably accompanied by liquid water-rich inclusions. These coexisting water-rich inclusions have ice-melting temperatures of −3 to −5 °C and clathrate-melting temperatures between +6 and +8 °C (Table 1), indicating lower salinity, with minor dissolved CO_2, than otherwise similar inclusion sets in the GGS 2b trails (Table 1). Most of the mixed H_2O–CO_2 inclusions are dominated by CO_2 vapour (Fig. 6b,c), and the liquid CO_2 annulus homogenizes

to vapour between 26 and 30 °C (Table 1). The mixed CO_2–H_2O inclusions and coexisting water-rich inclusions finally homogenize between 280 and 320 °C (Table 1). The secondary inclusion trails with co-existing water and mixed CO_2–H_2O inclusions are characteristic of fluid immiscibility during entrapment (Roedder, 1984; Craw *et al.*, 1993) as inferred above for the GGS 2b trails.

All glassy quartz boudin necks examined in this study have abundant late-stage irregularly shaped secondary water inclusions similar to those described above for the Gongto Glacier (GGS 2c; Table 1). Vapour-rich inclusions dominate, with relatively minor coexisting liquid-rich inclusions. Some of these late secondary trails contain only vapour-rich inclusions. The water inclusions homogenize between 280 and 345 °C, with coexisting liquid- and vapour-rich inclusions homogenizing at similar temperatures in this range (NBS 2b; Table 1). Many vapour-rich inclusions decrepitated before homogenization. Liquid-rich inclusions have ice-melting temperatures between −3 and −5 °C, and eutectic melting was not observed.

Late-metamorphic quartz in thrust fault zones

Primary inclusions are not preserved in milky quartz in the deformed veins (Fig. 5a,b), but some primary inclusions are present in glassy quartz which crosscuts this milky quartz (Fig. 5a). The primary inclusions in the glassy quartz (FZLG 1; Table 1) are petrographically and microthermometrically indistinguishable from early secondary inclusions in the milky quartz (FZLM 2; Table 1) and early secondary inclusions in the glassy quartz (FZLG 2a), and all three types will be described together here for brevity. These inclusions consist of mixtures of water and carbon dioxide that are commonly accompanied by liquid water-rich inclusions (Fig. 7a). Some secondary trails in both milky and glassy quartz do not have these coexisting liquid inclusions (Fig. 7b). Most of the mixed H_2O–CO_2 inclusions are dominated by CO_2 vapour (Fig. 7a,b), and the liquid CO_2 annulus homogenizes to vapour between 27 and 30 °C (Table 1). The mixed CO_2–H_2O inclusions and coexisting water-rich inclusions homogenize between 270 and 330 °C (Table 1). These homogenization data and visual estimates of volumetric proportion of CO_2 component (Roedder, 1984) imply bulk inclusion composition of 40–50 mol.% CO_2, and fluid density between 0.2 and 0.5 g cm^{-3} (Fig. 8a; Schwartz, 1989). The coexisting water-rich inclusions generally have ice-melting temperatures of −3 to −5 °C and clathrate-melting temperatures between +6 and +8 °C (Table 1), indicating low salinity and minor dissolved CO_2. The wide range of coexisting inclusion compositions in both primary and secondary occurrences in these veins is typical of fluid immiscibility during entrapment (Roedder, 1984; Craw *et al.*, 1993), as inferred for GGS 2b and NBS 2a (above).

One set of secondary inclusions in a sample of glassy quartz, from the same outcrop as Fig. 7(a,b) inclusions, has mixed CO_2–H_2O inclusions in which the CO_2 component is liquid-dominated (Fig. 7c; FZLG 2b, Table 1). The CO_2 component homogenizes to liquid between 28 and 31 °C and the inclusions, along with coexisting water-rich inclusions, finally homogenize between 280 and 300 °C (Table 1). These mixed CO_2–H_2O fluids are slightly denser (0.5–0.6 g cm^{-3}; Fig. 8a) than the vapour-dominated fluids described above (FZLG 2a). The relative timing relationships between these two fluid types is not known.

The most prominent secondary inclusions in glassy quartz occur as trails of irregularly shaped vapour-rich water inclusions (Fig. 7d). These inclusions are rarely accompanied by liquid-dominated water inclusions in the same trails. Water inclusions homogenize between 245 and 365 °C, with coexisting liquid- and vapour-rich inclusions homogenizing at similar temperatures in this range (Table 1). Many vapour-rich inclusions decrepitated before homogenization. Ice in vapour-rich inclusions melted at 0 °C, and ice in liquid-rich inclusions melted between 0 and −0.3 °C, and no CO_2 clathrates were observed.

Large irregular-shaped vapour-rich mixed CO_2–H_2O secondary inclusions occur in trails that cut across early secondary trails. The timing relationship between these large late inclusions and the large water vapour inclusions (FZLG 2c; Table 1) described above is not known. At room temperature, these mixed water and carbon dioxide vapour inclusions are indistinguishable from the above water vapour inclusions (FZLG 2c; Fig. 7d). On cooling, an annulus of CO_2 vapour develops around the water vapour margin between +16 and +11 °C (FZLG 2d; Table 1), and the inclusions then resemble those in Fig. 7(c). The fluids in these inclusions have lower density (*c.* 0.1 g cm^{-3}) than other mixed CO_2–H_2O fluids (above) and are 40–60 mol.% CO_2 (Fig. 8a). These fluids have clathrate-melting temperature of 10 °C (Table 1) and therefore have no dissolved salts.

Post-metamorphic hydrothermal veins near Pai

The quartz in these veins is prismatic and glassy, and primary inclusions are well-preserved. These primary inclusions (PHP 1; Table 1) are equant and distributed throughout clear quartz, and some inclusions have hexagonal outlines. The inclusions are liquid water with vapour bubbles that homogenize between 290 and 295 °C. Final ice-melting temperatures are −3 to −4 °C, with eutectic melting temperature near −23 °C.

All samples examined from this locality are dominated by large (> 50 μm) secondary inclusions that occur in irregular trains cutting across the crystals. These inclusions are predominantly water vapour, with a small liquid component around the rims (similar to FZLG 2c; Fig. 7d). Elongate small (< 20 μm) liquid water-rich inclusions rarely accompany the vapour-

rich inclusions in some inclusion trains, and most trains do not contain liquid-rich inclusions. Vapour-rich inclusions homogenize in a narrow range between 288 and 310 °C, and the rare coexisting liquid-rich inclusions homogenize between 290 and 296 °C. Ice-melting temperatures for all these water inclusions are 0 °C (PHP 2a; Table 1).

Similar large vapour-dominated inclusions to those described above (PHP 2a; Table 1), when observed at room temperature, develop an annulus of CO_2 vapour between $+15$ and $+12$ °C, as for the FZLG 2d inclusions described above (Table 1). These inclusions have ice-melting temperature of 0 °C, and clathrate-melting temperature of 10 °C (Table 1) and have no dissolved salts (see above).

Coexistence of liquid- and vapour-rich inclusion types is characteristic of boiling during entrapment (Roedder, 1984; Craw et al., 1994). The vein mineral assemblage quartz–adularia-bladed calcite that hosts these inclusions (Fig. 4b) forms in hydrothermal boiling zones (Simmons & Christenson, 1994; Craw, 1997), adding further support for the occurrence of boiling fluids. The liquid in this boiling system has density of c. 0.7 g cm^{-3} (Fig. 8a, inset). No vapour-rich inclusions in our samples have detectable dissolved salts, so the presence of dry steam (cf. Craw et al., 1997) cannot be confirmed. However, the abundant vapour-rich inclusions without coexisting liquid-rich inclusions means that dry steam cannot be fully discounted either. Such dry steam would have a density <0.1 g cm^{-3} (Fig. 8a, inset). Similar vapour-rich inclusions elsewhere in the Yarlung Tsangpo valley, in the thrust faults west of Pai (FZLG 2c, FZLG 2d; Table 1), could also represent zero-salinity dry steam, but this cannot be confirmed.

Lhasa block gneisses

Lower amphibolite facies metasedimentary gneisses on the margin of the gneiss complex contain inclusions dominated by carbon dioxide (Fig. 1). The inclusions are small (1–2 μm) and are scattered through quartz as irregular secondary trails. The inclusions are too small for detailed petrography or microthermometry, and it is not possible to determine if they have a film of water around their outer rims. A small vapour bubble forms on cooling to 0 to $+5$ °C. Hence, we can conclude merely that these inclusions are >90 vol.% carbon dioxide liquid, with density of c. 0.9 g cm^{-3} (Diamond, 2001). A detailed examination of the fluids in the rocks surrounding the core gneiss complex is beyond the scope of this study.

DISCUSSION

Comparison to other Himalayan fluid systems

Amphibolite facies gneisses in the central Himalaya are pervaded by CO_2-rich fluids (>80 mol.%; Boullier et al., 1991; Sachan et al., 2001), especially near the

Main Central Thrust (Fig. 1). This CO_2 is derived from decarbonation reactions associated with high-grade metamorphism and igneous intrusion (Boullier et al., 1991; Kerrick & Caldeira, 1998). The proportion of CO_2 decreases northwards in greenschist facies and lower-grade Tethyan rocks (Craw, 1990). Instead, the Tethyan rocks have abundant brines in early-formed fluid inclusions (Pecher, 1979; Craw, 1990; Singh & Sharma, 1997). In addition, saline warm and ambient springs emanate from subgreenschist Tethyan rocks (Craw, 1990). Both CO_2 and brines are diluted at shallow levels by incursion of surface water (Craw, 1990; Boullier et al., 1991). Hence, the eastern syntaxis core gneisses differ from those of the central Himalaya in having brines, not CO_2, as the principal fluid. However, gneisses on the margin of the eastern syntaxis core do have CO_2 as the principal fluid (Fig. 2).

Gneisses in and around the western syntaxis also have CO_2 as the principal fluid at depth (Craw et al., 1997). This CO_2 has been displaced by incursion of surface water in the core of the syntaxis at Nanga Parbat (Craw et al., 1994, 1997). Minor saline water occurs locally in association with the transition between deeper fluids and shallow water (Craw et al., 1997). However, brines are not as significant a part of the fluid system in gneisses at Nanga Parbat as they are in the eastern syntaxis. Instead, the Nanga Parbat massif is dominated in the upper 5 km by boiling water and dry steam (Craw et al., 1994, 1997). Immiscible water and mixed CO_2–H_2O fluids occur rarely within this zone (Craw et al., 1994). As outlined above, dry steam is minor or absent from the eastern syntaxis. However, boiling water is common at shallow levels, and immiscible water and mixed CO_2–H_2O fluids dominate at intermediate depths (above).

Physical conditions of fluid entrapment

The widespread evidence of fluid immiscibility (including boiling) during entrapment of many of the inclusions described above (Fig. 2) allows estimates of both temperature and fluid pressure during entrapment (Roedder, 1984; Bakker & Diamond, 2000; Diamond, 2001). The simplest system to apply this approach are the late-stage water inclusions that have evidence of boiling (above). Coexistence of both liquid and vapour inclusions with similar homogenization temperatures implies that entrapment temperature is the same as homogenization temperature (Roedder, 1984), and these inclusions were trapped between 290 and 365 °C (Fig. 8a, inset). This range of temperatures occurs within individual samples, between samples in the Yarlung Tsangpo valley where these inclusion types are most common, and between samples in the Gongto Glacier area (Fig. 2). This range of boiling temperatures implies fluid pressures of between 80 and 200 bar (Fig. 8a, inset).

Mixed H_2O–CO_2 inclusions coexisting with liquid-rich water inclusions represent entrapment of

immiscible fluids in the CO_2–H_2O system, and again the entrapment temperature range is equal to the final homogenization temperature range of 280–320 °C (Table 1). Estimation of fluid pressure from phase equilibria (Fig. 8b) is less precise than for boiling water, but fluid pressures between 200 and 600 bar are implied. The lower end of the observed temperature range, and the higher end of the estimated fluid pressure range is defined by a single sample containing inclusions with relatively dense CO_2 (above; Fig. 7d). Hence, we conclude that there has been widespread CO_2–H_2O fluid immiscibility at 290–320 °C and *c*. 200–500 bar fluid pressure through the core gneiss complex, and more localized similar immiscibility at slightly greater fluid pressures and lower temperatures. Immiscibility of concentrated brines and mixed CO_2–H_2O fluids (e.g. Fig. 6c) at similar temperatures implies entrapment in the 200–400 bar fluid pressure range also (Bodnar, 2003).

Mixed water and carbon dioxide vapour inclusions may imply fluid immiscibility during entrapment at 280–320 °C (FZLG 2d, PHP 2b; Table 1) at fluid pressure near 200 bar (Fig. 8b). However, as no coexisting liquid-rich inclusions occur, immiscibility cannot be confirmed (see above). Instead, entrapment of these inclusions may have occurred at higher temperatures in the vapour (dry steam) field, similar to water vapour inclusions, along or near the 0.1 g cm^{-3} isochore (e.g. Fig. 8a, inset). Consequently, it is not possible to define entrapment temperature or fluid pressure of these possible dry steam fluids (cf. Craw *et al.*, 1997).

Some of the most concentrated brines were trapped as primary inclusions in veins which contain amphibolite facies metamorphic minerals (Figs 4a & 6a). These inclusions homogenize near 500 °C (Table 1). The slopes of isochores in temperature–fluid pressure space for such highly saline and chemically complex solutions are not known in detail, but isochores typically have slopes of *c*. 1 bar °C^{-1} (Bodnar, 2003). A major pressure correction is required for the homogenization temperature of these inclusions to determine temperature of entrapment, and the magnitude of this correction is unknown without pressure constraints. However, it is concluded that entrapment occurred during amphibolite facies metamorphism (>500 °C) under brittle–ductile conditions in which fractures formed and subsequent vein infills were boudinaged (Fig. 4a).

Temperature–depth estimates

Fluid pressure estimates of the previous section can be used, with assumptions, to estimate depths of entrapment. The required assumptions preclude precise estimations for individual samples, so we focus instead on the most widespread inclusion type with the most consistent temperatures of entrapment. These are the coexisting immiscible water-rich and

mixed CO_2–H_2O fluids that were trapped at 300 ± 20 °C (Table 1) between 200 and 500 bar fluid pressure (Fig. 8b). It is assumed that this widespread fluid type and narrow temperature range of entrapment represents a regionally uniform feature of the thermal structure of the gneiss complex, and that the fluid temperature equalled the rock temperature at this level. It is also assumed that the fluid pressure regime was hydrostatic during the fracturing and hydrothermal activity that resulted in entrapment of these secondary inclusions. Conversion of fluid pressure to depth in this hydrostatic regime requires assumption of an average overlying fluid density, which is estimated to be *c*. 0.8 g cm^{-3} (Fig. 8a, inset). From these assumptions, depth can be estimated for the 300 °C isotherm to be between 2.5 and 6.2 km. While these estimates are imprecise, they show that the thermal gradient in the core gneiss complex averages >50 °C km^{-1} in the upper few kilometres, possibly as high as 120 °C km^{-1}. Clearly, the gneiss complex must be a shallow thermal anomaly, consistent with the abundant hot springs in the area.

Boiling waters such as those that formed the veins in Fig. 4(b) was trapped at 340–360 °C, at lower fluid pressure (<200 bar) than the above immiscible fluids (Fig. 8a, inset). Using these observations and the assumptions of the previous paragraph, a much higher geothermal gradient (>140 °C km^{-1}) can be calculated. However, we suggest that this is unrealistically high, and that the boiling water was hotter than the surrounding rock. Shallow penetration of hot or boiling water out of thermal equilibrium with the host rock is a common phenomenon in the area, appearing at the surface as hot springs (Fig. 2). It is also suggested that the mixed water and carbon dioxide vapour inclusions (generations FZLG 2d and PHP 2b, Table 1; Fig. 8a,b) may have been out of thermal equilibrium with the host rock, although the thermal gradient implied by these latter fluids (>100 °C km^{-1}) falls into the upper part the range of estimates in the previous paragraph.

Potassium–argon and argon–argon dating of biotite in the eastern syntaxis core gneisses yield ages as low as 1.2 Ma (Zhang *et al.*, 1981). The closure temperature for argon in biotite is *c*. 300 °C (Harrison *et al.*, 1985). Hence, this biotite has been exhumed from between 2.5 and 6.2 km depth (above) over 1.2 Myr. These observations imply that the rocks are being exhumed at between 2 and 5 mm year^{-1}. Burg *et al.* (1997) estimated a similar exhumation rate (3–5 mm year^{-1}) for the core gneisses over the past 2 Myr based on fission track data.

Fluid compositional evolution

The core gneiss complex has a long metamorphic history through the Tertiary and probably earlier (Booth *et al.*, 2004). Hence, the rocks have undergone thorough devolatilization in their early history. Amphibolite

facies gneisses with similar complex metamorphic histories elsewhere in the Himalaya typically retain only CO_2-rich fluid after amphibolite facies metamorphism (see above). We suggest that the carbon dioxide-rich fluid observed in rocks on the margins of the core gneiss complex (Fig. 2) is representative of the last metamorphic fluid in these rocks. These gneisses have since been rapidly uplifted from metamorphic depths over the past 10 Myr (Burg *et al.*, 1997, 1998), and the post-metamorphic fluids now observable in inclusions in veins in the gneisses (described above) represent remnants of an evolving fluid regime associated with the growth of the high mountains of the eastern syntaxis.

The structurally earliest fluids in this evolving fluid system are the concentrated brines that accompanied initial vein development under amphibolite facies conditions, and persisted as the rocks became more generally brittle during uplift and cooling. These brines have clearly displaced or diluted the presumed CO_2 metamorphic fluid. The source of the concentrated brines is unknown, but Tethyan sedimentary rocks elsewhere in the Himalaya have abundant brines (see above). Tethyan rocks almost certainly covered the core gneisses of the eastern syntaxis before the late Tertiary–Recent uplift and exhumation of the complex, and these presumably contained brines similar to those of the central Himalaya. It is possible that the marble and associated metasedimentary gneisses in the Gongto Glacier area (Fig. 3) are a slice of Tethyan sediments incorporated tectonically into the core gneisses during early stages of uplift, and contributed brines at the same time. Alternatively, younger marine sediments that are locally still preserved on the Lhasa block to the north probably overlay the eastern syntaxis until the recent exhumation (Leeder *et al.*, 1988; Yin *et al.*, 1988), and these sediments may have contributed brines to the underlying basement. Brines in sedimentary rocks have relatively high density (>1 g cm^{-3}) compared with the fluids in the underlying metamorphic rocks and may have undergone gravity-driven migration downwards into the underlying gneisses, to mix with and/or displace pre-existing fluids.

The Gongto Glacier gneisses were progressively flushed by surface water during uplift and exhumation, so that the brines were steadily diluted from c. 60 wt% salinity at >500 °C to essentially zero salinity at c. 250 °C (Table 1). Minor carbon dioxide, possibly that displaced by the downward-percolating brines, also became incorporated into the diluting water around the 300 °C level, but this became less significant at shallower levels. Similar brine incursion may have occurred in the Namche Barwa gneisses, although the range of observed salinities is less than at the Gongto Glacier (Table 1). The boiling water inclusions that are particularly common in the Yarlung Tsangpo valley samples were presumably linked to surface hot spring systems of the type that are still common in that valley. Alteration of host rock amphibolite facies

mineralogy to greenschist facies mineralogy (epidote + chlorite; Fig. 5a) and lower temperature clay + calcite assemblages in thrust fault gouges west of Pai (Figs 2 & 5b) reflect water–rock interaction of this shallow-level water-dominated fluid system.

Inferred large-scale fluid migration paths outlined above are depicted in a cross-section through the core gneiss complex (Fig. 9a). This diagram depicts original metamorphic CO_2 (in deep ductile rocks) that has been displaced by incursion of brines from the now-eroded marine sedimentary rocks. Topographically driven surface waters are diluting brines and dissolving remnant carbon dioxide, then returning to the surface as shallow-level hot water and hot/warm springs. Now that marine sediment cover has been removed, the amount of brine in the gneiss complex will progressively decrease with further exhumation and surface water dilution.

Widespread fluid immiscibility occurs near to the 300 °C isotherm that is located in Fig. 9(a) in the middle of the depth range estimated above from fluid inclusion data (Fig. 8b). Localized upward flux of water hotter than the surrounding rocks gives boiling zones at shallow levels, possibly with minor dry steam. The inferred fluid compositional evolution for a single Gongto Glacier rock specimen (e.g. Fig. 4a) is shown with a heavy line in Fig. 9(b). The initial dashed portion represents inferred incursion of brines into CO_2-bearing metamorphic rocks. Summarized fluid evolutionary trends for the central Himalaya and Nanga Parbat in the western syntaxis (described above) are shown in Fig. 9(b) for comparison.

Thermal modelling

Evidence is presented above for the existence of a major shallow thermal anomaly in the eastern syntaxis, similar to that of the western syntaxis (Winslow *et al.*, 1994; Craw *et al.*, 1997; Zeitler *et al.*, 2001; Koons *et al.*, 2002). The two-dimensional structure of this thermal anomaly is sketched in Fig. 9(a), with the 300 °C isotherm and the position of the brittle–ductile transition both undulating. The geometry and spacing of undulating isotherms, and consequently the variations in thermal gradient, arise from two principal features: steep topography, and advection of hot rocks (Craw *et al.*, 1994; Koons *et al.*, 2002). In this section, two thermal models are presented that compare the different thermal structures that arise from these principal features of active mountain uplift.

In order to examine these different thermal structures, the transient conductive/advective heat flow equation is approximated to:

$$\frac{\partial T}{\partial t} = \kappa \nabla^2 T + \mathbf{V} \nabla T + A(x,y,z)$$

where κ is the thermal diffusivity (here $= 10^{-6}$ m^2 s^{-1}; Koons *et al.*, 2002), $\mathbf{V}$ is 3D velocity field, and $A(x,y,z)$ is a radioactive source term, through a Lagrangian
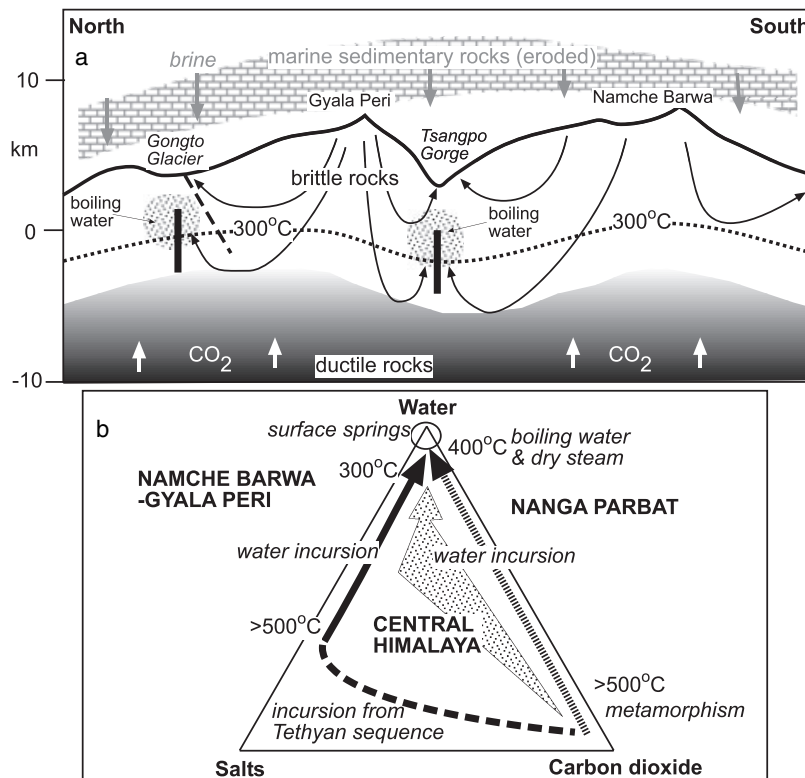
Fig. 9. Summary diagram for fluid sources and compositional evolution in the Namche Barwa and Gyala Peri massifs. (a) Sketch cross-section through the massif, showing inferred fluid pathways. The position of the 300 °C isotherm is indicated (dotted line), with uncertainties beneath Gongto Glacier and Yarlung Tsangpo gorge shown as vertical black bars. Boiling zones in which fluid temperature exceeds rock temperature are stippled. (b) Ternary diagram showing evolution of fluid compositions with respect to principal chemical components. Evolutionary paths for the central Himalaya and Nanga Parbat (western syntaxis) are shown for comparison.

explicit algorithm (Cundall & Board, 1988; ITASCA, 1997). The upper surface is derived from GTOPO30 topography (Fig. 10a) gridded to *c.* 1 km spacing over a region of *c.* 110 km × 88 km extending 20 km below sea level (Fig. 10b). The rocks are assumed to be isotropic with respect to heat flow, and uniform over the whole problem domain. The Namche Barwa and Gyala Peri massifs and adjacent Lhasa Block include a wide range of high-grade metasedimentary gneisses and granitoids with widely varying structural orientations. Hence, this assumption of isotropic uniformity is an approximation, but geological variations are commonly at the km scale and are too poorly known to allow more detailed and realistic inputs to the model. Such detailed inputs are beyond the scope of this study. Our initial model (Fig. 10c) shows the influence on the thermal structure of the extreme relief in the syntaxial region, without any rock advection. For this model, basal heat flow is 40×10^{-3} mW m^{-2} and radioactive heat source is 1.5×10^{-6} W m^{-3}. The topographic surface is maintained at a fixed temperature of 0 °C, the sides of the model have no net flow, and the model was run to a steady state. The thermal map in Fig. 10(c) is drawn as a horizontal slice through the model at sea level. The strong effects on local thermal gradients of up to 7 km of relief is readily apparent in Fig. 10(c), which shows prominent thermal highs under the high mountains and lows beneath the valleys. However, the near-surface thermal gradient

beneath the high mountains is only 15 and 30 °C km^{-1} beneath the deep valleys.

There is insufficient velocity information for this region to construct an advective thermal model of the kind developed for the western syntaxis (Craw *et al.*, 1994; Koons *et al.*, 2002). Instead, a conductive thermal anomaly was produced by numerical maintenance of the 400 °C isotherm at a depth of 7 km over an area of 40 km × 40 km, coinciding with the Gyala Peri and Namche Barwa massifs. This thermally perturbed model is conditioned to meet the fluid inclusion observation of *c.* 300 °C near sea level (Fig. 9a). The non-linear advective and heat source terms are gathered into a single value in the advective region. This thermal perturbation in the model is intended to represent development of a shallow conductive thermal anomaly during rapid uplift (Koons, 1987; Craw *et al.*, 1994) without predefining a velocity field. In this model (Fig. 10d), the thermal highs beneath the mountains are strongly enhanced compared with the topographic model (Fig. 10c). Local horizontal thermal gradients are steepened to as high as 15 °C km^{-1} in the thermally perturbed model (Fig. 10d), and vertical thermal gradients are typically near 70 °C km^{-1} in the Tsangpo gorge in this model (Fig. 10d,e; cf. Fig. 9a). Thermal perturbations from fluid flow are undoubtedly present (Fig. 2), but these are small at the scale of this model, and they are ignored here (cf. Craw *et al.*, 1994). A preliminary mechanical model to accompany this ad-
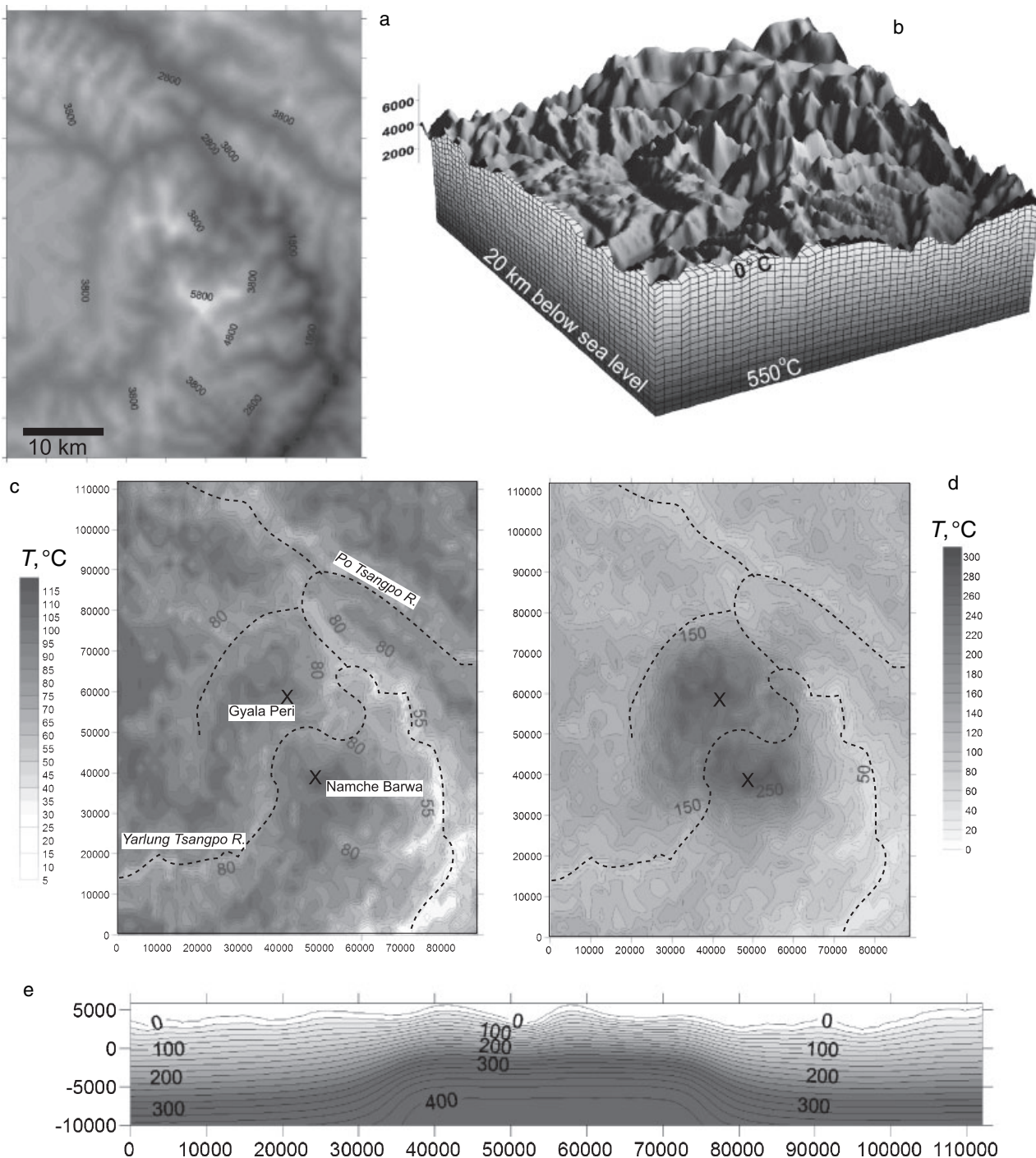
Fig. 10. Thermal models for the Namche Barwa and Gyala Peri massifs (see text for explanations). (a) Topographic map of the modelled part of the massif; see (c) and (d) for localities. Darker colours are lower elevations. (b) Block diagram of the model domain, viewed from the NW. The vertical scale is exaggerated. (c) Model results with no thermal perturbation, shown as a horizontal slice through Fig. 10(b) at sea level. Rock temperatures are contoured with 5 °C intervals, as indicated in the scale bar to the left. (d) Model results with thermal perturbation, shown as a horizontal slice through Fig. 10(b) at sea level. Rock temperatures are contoured with 20 °C intervals, as indicated in the scale bar to the right. (e) Vertical cross-section (south to north) through the model domain for the model with thermal perturbation (Fig. 10d), showing the strong elevation of isotherms and high near-surface thermal gradients.

vective thermal model has been presented by Koons *et al.* (2002), and a full advective model of thermal perturbations accompanying rock uplift will be devel-oped in the future when velocity data from global positioning system measurements have been refined sufficiently to provide full velocity constraints.

CONCLUSIONS

The Namche Barwa and Gyala Peri massifs are being uplifted at 2–5 mm year^{-1} in the eastern Himalayan syntaxis. A near-surface conductive thermal anomaly has developed beneath the massifs, centred on the deep gorge of the Yarlung Tsangpo River. Numerous warm and hot springs emanate at the surface, reflecting widespread and deep penetration of meteoric water into the thermally anomalous crust. The 300 °C isotherm lies between 2.5 and 6.2 km depth below surface, and the near-surface average thermal gradient exceeds 50 °C km^{-1} beneath valleys. The high near-surface temperatures can be modelled with the equivalent of a mass of hot rock (400 °C) at 7 km depth. This hot rock mass is presumed to be tectonically advected into the massif at rates faster than the rocks can cool.

Gneisses of the massif contained a metamorphic fluid with a high proportion (>90%) of CO_2 prior to uplift, and were overlain by Tethyan or younger marine sedimentary rocks. Downward percolation of brines from the sedimentary rocks displaced much of the CO_2, and late-metamorphic veins (500 °C) contain fluid inclusions with 60 wt% dissolved salts. Some of these fluid inclusions contain several daughter crystals, including Ca, Na, K and Fe chlorides. Topography-driven incursion of meteoric water during uplift resulted in brine dilution down to the brittle–ductile transition. Post-metamorphic hydrothermal alteration of the rock mass was structurally controlled and localized, but was widespread. Shallow hydrothermal fluids are dominated by liquid water with low salinity and minor CO_2. There is extensive evidence for fluid immiscibility in the upper 6 km, including boiling water (up to 350 °C) at shallow levels (<3 km).

The Namche Barwa–Gyala Peri advective thermal anomaly and associated post-metamorphic hydrothermal system resembles a similar system at Nanga Parbat in the western Himalayan syntaxis. However, shallow rock temperatures are lower in the eastern syntaxis than at Nanga Parbat, and this, combined with the high rainfall in the east, precludes widespread development of dry steam that is seen at Nanga Parbat. In contrast, metamorphic rocks in the central Himalaya have higher CO_2 content of late-stage fluids, and lower temperature and more localized shallow-level hydrothermal systems, compared with the syntaxes.

REFERENCES

Anderson, A. J. & Mayanovic, R. A., 2003. Electron, nuclear, and X-ray probe microanalysis of fluid inclusions. In: *Fluid Inclusions: Analysis and Interpretation* (eds Samson, I., Anderson, A. & Marshall, D.), *Mineralogical Association of Canada Short Course*, **32**, 323–351.

Bakker, R. J. & Brown, P. E., 2003. Computer modelling in fluid inclusion research. In: *Fluid Inclusions: Analysis and Interpretation* (eds Samson, I., Anderson, A. & Marshall, D.), *Mineralogical Association of Canada Short Course*, **32**, 175–212.

Bakker, R. J. & Diamond, L. W., 2000. Determination of the composition and molar volume of H$_2$O–CO$_2$ fluid inclusions by microthermometry. *Geochimica et Cosmoschimica Acta*, **64**, 1753–1764.

Bhattarai, D. R., 1980. Some geothermal springs of Nepal. *Tectonophysics*, **62**, 7–11.

Blencoe, J. G., Naney, M. T. & Anovitz, L. M., 2001. The CO$_2$–H$_2$O system: III. A new experimental method for determining liquid-vapor equilibria at high subcritical temperatures. *American Mineralogist*, **86**, 1100–1111.

Bodnar, R. J., 2003. Introduction to aqueous electrolyte fluid inclusions. In: *Fluid Inclusions: Analysis and Interpretation* (eds Samson, I., Anderson, A. & Marshall, D.), *Mineralogical Association of Canada Short Course*, **32**, 81–100.

Bodnar, R. J., Sterner, S. M. & Hall, D. M., 1989. SALTY: a FORTRAN program to calculate compositions of fluid inclusions in the system NaCl-KCl-H$_2$O. *Computer and Geosciences*, **15**, 19–41.

Booth, A. L., Zeitler, P. K., Kidd, W. S. F. et al., 2004. U–Pb zircon constraints on the tectonic evolution of southeastern Tibet, Namche Barwa area. *American Journal of Science*, **304**, 889–929.

Boullier, A.-M., France-Lanord, C., Dubessy, J., Adamy, J. & Champenois, M., 1991. Linked fluid and tectonic evolution in the High Himalaya mountains (Nepal). *Contributions to Mineralogy and Petrology*, **107**, 358–372.

Brown, P. E. & Hagemann, S. G., 1995. MacFlinCor and its application to fluids in Archean lode-gold deposits. *Geochimica et Cosmochimica Acta*, **59**, 3943–3952.

Burg, J.-P., Davy, P., Nievergelt, P. et al., 1997. Exhumation during crustal folding in the Namche Barwa syntaxis. *Terra Nova*, **9**, 53–56.

Burg, J. P., Nievergelt, P., Oberli, F. et al., 1998. The Namche-Barwa syntaxis: evidence for exhumation related to compressional crustal folding. *Journal of Asian Earth Sciences*, **16**, 239–252.

Chamberlain, C. P., Koons, P. O., Meltzer, A. S. et al., 2002. Overview of hydrothermal activity associated with active orogenesis and metamorphism: Nanga Parbat, Pakistan Himalaya. *American Journal of Science*, **302**, 726–748.

Craw, D., 1990. Fluid evolution during uplift of the Annapurna Himal, Central Nepal. *Lithos*, **24**, 137–150.

Craw, D., 1997. Fluid inclusion evidence for geothermal structure beneath the Southern Alps, New Zealand. *New Zealand Journal of Geology and Geophysics*, **40**, 43–52.

Craw, D., Teagle, D. A. H. & Belocky, R., 1993. Fluid immiscibility in late-Alpine gold-bearing veins, Eastern and Northwestern European Alps. *Mineralium Deposita*, **28**, 28–36.

Craw, D., Koons, P. O., Winslow, D., Chamberlain, C. P. & Zeitler, P., 1994. Boiling fluids in a region of rapid uplift,

Nanga Parbat massif, Pakistan. *Earth and Planetary Science Letters*, **128**, 169–182.

Craw, D., Chamberlain, C. P., Zeitler, P. K. & Koons, P. O., 1997. Geochemistry of a dry steam geothermal zone formed during rapid uplift of Nanga Parbat, northern Pakistan. *Chemical Geology*, **142**, 11–22.

Cundall, P. & Board, M., 1988. A microcomputer program for modeling of large-strain plasticity problems. In: *Numerical Methods in Geomechanics* (ed. Swododa, C.), Proceedings of the 6th International Conference on Numerical Methods in Geomechanics, pp. 101–108. Balkemapp, Innsbruck, Austria.

Diamond, L. W., 2001. Review of the systematics of CO_2–H_2O fluid inclusions. *Lithos*, **55**, 69–99.

Diamond, L. W., 2003. Introduction to gas-bearing aqueous fluid inclusions. In: *Fluid Inclusions: Analysis and Interpretation* (eds Samson, I., Anderson, A. & Marshall, D.), *Mineralogical Association of Canada Short Course*, **32**, 101–158.

Gansser, A., 1964. *Geology of the Himalayas*. Wiley Interscience, London, 289 pp.

Harrison, T. M., Duncan, I. & McDougall, I., 1985. Diffusion of ^{40}Ar in biotite: temperature, pressure, and compositional effects. *Geochimica et Cosmochimica Acta*, **49**, 2461–2468.

Hochstein, M. P. & Regenauer-Lieb, K., 1998. Heat generation associated with collision of two plates: the Himalayan geothermal belt. *Journal of Volcanology and Geothermal Research*, **83**, 75–92.

Hochstein, M. P. & Yang, Z., 1995. The Himalayan Geothermal Belt (Kashmir, Tibet, West Yunnan). In: *Terrestrial Heat Flow and Geothermal Energy in Asia* (eds Gupta, M. L. & Yamamo, M.), pp. 331–368. Oxford and IBH Publishing, New Delhi.

Hodges, K. V., Wobus, C., Ruhl, C., Schildgen, T. & Whipple, K., 2004. Quaternary deformation, river steepening, and heavy precipitation at the front of the Higher Himalayan ranges. *Earth and Planetary Science Letters*, **220**, 379–389.

Hubbard, M. S., 1989. Thermobarometric constraints on the thermal history of the Main Central Thrust Zone and Tibetan Slab, eastern Nepal Himalaya. *Journal of Metamorphic Geology*, **7**, 19–30.

ITASCA, 1997. *FLAC3D (Fast Lagrangian Analysis of Continua in 3 Dimensions)*. ITASCA, Minneapolis, MN, USA.

Kerrick, D. M. & Caldeira, K., 1998. Metamorphic CO_2 degassing from orogenic belts. *Chemical Geology*, **145**, 213–232.

Koons, P. O., 1987. Some thermal and mechanical consequences of rapid uplift: an example from the Southern Alps. *Earth and Planetary Science Letters*, **86**, 307–319.

Koons, P. O., Zeitler, P. K., Chamberlain, C. P., Craw, D. & Meltzer, A. S., 2002. Mechanical links between erosion and metamorphism in Nanga Parbat, Pakistan Himalaya. *American Journal of Science*, **302**, 749–773.

Leeder, M. R., Smith, A. B. & Yin, J., 1988. Sedimentology, palaeoecology, and palaeoenvironmental evolution of the 1985 Lhasa to Golmud Geotraverse. *Philosophical Transactions of the Royal Society of London A*, **327**, 107–143.

Liu, Y. & Zhong, D., 1997. Petrology of high-pressure granulites from the eastern Himalayan syntaxis. *Journal of Metamorphic Geology*, **15**, 451–466.

Maaskant, P., 1986. Electron probe microanalysis of unopened fluid inclusions, a semiquantitative approach. *Neues Jahrbuch fur Mineralogie Monatschefte*, **7**, 297–304.

Pecher, A., 1979. Les inclusions fluids dans des quartz d'exsudation de la zone du MCT himalayen au Nepal central: donnees sur la phase fluid dans une grande zone de cisaillement crustal. *Bulletin de Mineralogie*, **102**, 537–554.

Roedder, E., 1984. *Fluid Inclusions. Reviews in Mineralogy 12*. Mineralogical Society of America, Washington, DC, 644 pp.

Sachan, H. K., Sharma, R., Sahai, A. & Gururajan, N. S., 2001. Fluid events and exhumation history of the Main Central Thrust zone, Garwhal Himalaya (India). *Journal of Asian Earth Science*, **19**, 207–221.

Schwartz, M. O., 1989. Determining phase volumes of mixed CO_2–H_2O inclusions using microthermometric measurements. *Mineralium Deposita*, **24**, 43–47.

Simmons, S. F. & Christenson, B. W., 1994. Origins of calcite in a boiling geothermal system. *American Journal of Science*, **294**, 361–400.

Singh, K. & Sharma, R., 1997. Magnesite mineralization along the Chamba Thrust, Himachal Himalaya; structural control and depositional environment using fluid inclusions. *Journal of the Geological Society of India*, **49**, 289–296.

Tong, W. & Zhang, J., 1981. Characteristics of geothermal activities in Xizang Plateau and their controlling influence on Plateau's tectonic model. In: *Geological and Ecological Studies of the Quinghai-Xizang Plateau*, pp. 841–846. Gordon and Breach, New York.

Vanko, D. A., Bodnar, R. J. & Sterner, S. M., 1988. Synthetic fluid inclusions. VIII. Vapor-saturated halite solubility in part of the system $NaCl$–$CaCl_2$–H_2O with application to fluid inclusions from oceanic hydrothermal systems. *Geochimica et Cosmochimica Acta*, **52**, 2451–2456.

Winslow, D. M., Zeitler, P. K., Chamberlain, C. P. & Hollister, L. S., 1994. Direct evidence for a steepened geotherm under conditions of rapid denudation, Pakistan Himalaya. *Geology*, **22**, 1075–1078.

Yin, J., Xu, J., Liu, C. & Li, H., 1988. The Tibetan Plateau: regional stratigraphic context and previous work. *Philosophical Transactions of the Royal Society of London A*, **327**, 5–52.

Zeitler, P. K., Meltzer, A. S., Koons, P. O., *et al.*, 2001. Erosion, Himalayan geodynamics, and the geomorphology of metamorphism. *GSA Today*, **11**, 4–9.

Zhang, Y.-Q., Dai, T.-M. & Hong, A.-S., 1981. Isotopic geochronology of granitoid rocks in southern Xizang plateau. In: *Proceedings, Symposium. Qinghai Xizang (Tibet) Plateau*, pp. 483–495. Science Press, Beijing.

Zhang, Z. G., Liu, Y. H., Qang, T. W., Yang, H. X. & Xu, B. C., 1992. *Geology of the Namche Barwa region*. Chinese Science Press, Beijing, 185 pp.